

# Multiwavelength monitoring of NGC 1275 over a decade: Evidence of a shift in synchrotron peak frequency and long-term multi-band flux increase

Sanna Gulati,<sup>1</sup> Debbijoy Bhattacharya,<sup>1</sup> ★ Subir Bhattacharyya<sup>2,3</sup>

Nilay Bhatt<sup>2</sup>, C. S. Stalin<sup>4</sup> and V. K. Agrawal<sup>5</sup>

<sup>1</sup>Manipal Centre for Natural Sciences, Centre of Excellence, Manipal Academy of Higher Education, Manipal - 576104, India

<sup>2</sup>Bhabha Atomic Research Centre, Mumbai - 400085, India

<sup>3</sup>Homi Bhabha National Institute, Anushaktinagar, Mumbai - 400094, India

<sup>4</sup>Indian Institute of Astrophysics, Bangalore - 560034, India

<sup>5</sup>Space Astronomy Group, U R Rao Satellite Centre, Bangalore - 560017, India

Accepted XXX. Received YYY; in original form ZZZ

## ABSTRACT

We carried out a detailed study of the temporal and broadband spectral behaviour of one of the brightest misaligned active galaxies in  $\gamma$ -rays, NGC 1275 utilising 11 years of *Fermi*, and available *Swift* and *AstroSat* observations. Based on the cumulative flux distribution of the  $\gamma$ -ray lightcurve, we identified four distinct activity states and noticed an increase in the baseline flux during the first three states. Similar nature of the increase in the average flux was also noticed in X-ray and UV bands. A large flaring activity in  $\gamma$ -rays was noticed in the fourth state. The source was observed twice by *AstroSat* for shorter intervals ( $\sim$ days) during the longer observing periods ( $\sim$ years) state 3 and 4. During *AstroSat* observing periods, the source  $\gamma$ -ray flux was higher than the average flux observed during longer duration states. The increase in the average baseline flux from state 1 to state 3 can be explained considering a corresponding increase of jet particle normalisation. The inverse Comptonisation of synchrotron photons explained the average X-ray and  $\gamma$ -ray emission by jet electrons during the first three longer duration states. However, during the shorter duration *AstroSat* observing periods, a shift of the synchrotron peak frequency was noticed, and the synchrotron emission of jet electrons well explained the observed X-ray flux.

**Key words:** galaxies: active — galaxies: jets — gamma-rays: galaxies — X-rays: galaxies — quasar: individual (NGC 1275)

## 1 INTRODUCTION

NGC 1275 is one of the brightest nearby radio galaxies ( $z = 0.0176$ ; Falco et al. 1999) situated at the centre of the Perseus cluster. The optical spectra of this galaxy exhibit strong emission lines which are a typical feature of Seyfert galaxies (Humason 1932; Khachikian & Weedman 1974). However, in the radio band, this source is classified as a Fanaroff-Riley type I (FR I type) radio galaxy with a compact central source and an extended jet (e.g., Vermeulen et al. 1994; Asada et al. 2006; Buttiglione et al. 2010).

NGC 1275 (4FGL J0319.8 + 4130) is one of the brightest misaligned active galaxies in  $\gamma$ -rays. Abdo et al. (2009) reported the discovery of high energy  $\gamma$ -ray emission from NGC 1275 utilising the first few months of observations from the Large Area Telescope (LAT) onboard the *Fermi*  $\gamma$ -ray space telescope (*Fermi*).

Evidence of variability, in both, long (Kataoka et al. 2010; Dutson et al. 2014) as well as short timescales with large flaring activities (Donato et al. 2010; Brown & Adams 2011; Ciprini 2013; Pivato & Buson 2015; Baghmany et al. 2017; Kushwaha et al. 2017; Tanada et al. 2018; Chitnis et al. 2020; Ghosal et al. 2020) in  $\gamma$ -rays was noticed in this source. NGC 1275 was also detected by Major Atmospheric Gamma Imaging Cherenkov (*MAGIC*) telescope and Very Energetic Radiation Imaging Telescope Array System (*VERITAS*) in very high energy  $\gamma$ -rays (Aleksić et al. 2012, 2014; Benbow & VERITAS Collaboration 2015; Mirzoyan 2016, 2017; Mukherjee & VERITAS Collaboration 2016, 2017; MAGIC Collaboration et al. 2018). Though earlier *MAGIC* observations showed marginal flux variation in monthly timescales, MAGIC Collaboration et al. (2018) reported a presence of significant variation in “day-by-day”  $\gamma$ -ray lightcurve.

NGC 1275 was studied in hard X-ray band using observations from Nuclear Spectroscopic Telescope Array - *NuS-*

★ E-mail: debbijoy.b@manipal.edu

TAR (Tanada et al. 2018; Rani et al. 2018; Chitnis et al. 2020). Rani et al. (2018) found that the emission above 20 keV is dominated by a non-thermal component with possible jet origin. NGC 1275 also exhibits correlated variability in different wavebands (Aleksić et al. 2014; Fukazawa et al. 2018). The broadband spectral energy distribution (SED) of NGC 1275 has been explained by one-zone synchrotron self Compton model (Abdo et al. 2009; Aleksić et al. 2014; Fukazawa et al. 2018; Tanada et al. 2018) or a structured jet (Tavecchio & Ghisellini 2014).

In this work, we have carried out a long-term study of NGC 1275 in  $\gamma$ -rays utilising 11 years of *Fermi*-LAT observations and identified different activity states. This source was also observed in X-rays, UV and/or optical band by *Swift*-XRT and *Swift*-UVOT multiple times during *Fermi* observing period. India’s first multi-wavelength astronomical observatory “*AstroSat*” (Agrawal 2006; Singh et al. 2014; Rao et al. 2016), also observed the source twice. *AstroSat* is capable of observing the sky simultaneously over a wide range of energies covering from near-UV (NUV) and far-UV (FUV) bands using the Ultra-Violet Imaging Telescope (UVIT; Kumar et al. 2012; Tandon et al. 2017), soft X-ray band with the Soft X-ray Telescope (SXT; Singh et al. 2017) to the hard X-ray band with the Large Area X-ray Proportional Counter (LAXPC; Yadav et al. 2016b; Antia et al. 2017) and Cadmium-Zinc-Telluride Imager (CZTI; Vadawale et al. 2015; Rao et al. 2017).

We have carried out construction and modelling of average broadband SEDs during different states as identified in the  $\gamma$ -ray light curve and during *AstroSat* observing periods to understand the long term behaviour of this source. Details of the analysis of multi-wavelength data used in this work are given in Section 2. In Section 3, we discuss our findings, followed by a conclusion in Section 4.

## 2 DATA ANALYSIS AND RESULTS

### 2.1 GeV DATA

We used the  $\gamma$ -ray data from *Fermi*-LAT (Atwood et al. 2009) covering the period from 2008-08-04 to 2019-08-04 (11 years) in the energy range from 100 MeV to 100 GeV. The data reduction is performed using the FermiTools version 1.2.23. The current version of *Fermi*-LAT data, pass 8 P8R3, was used for analysis (Bruehl et al. 2018). Instrument Response Function (IRF) P8R3\_SOURCE\_V2 was used for source class event selection. A  $15^\circ \times 15^\circ$  region of interest (ROI) centred at NGC 1275 was defined, and standard cuts were applied to select the good time intervals ( $z_{\max} < 90^\circ$ , DATA\_QUAL > 0 and LAT\_CONFIG == 1). Fermipy version 0.19.0 (Wood et al. 2017) was used to calculate the light curve and spectra using binned likelihood analysis. A spatial binning of  $0.1^\circ \text{ pixel}^{-1}$  and eight logarithmically-spaced energy bins per decade were chosen. Our initial model, generated using `make4fglxml.py`<sup>1</sup>, consists of all  $\gamma$ -ray point sources within  $20^\circ$  of the ROI centre included in the 4FGL-DR2 catalogue (Ballet et al. 2020) and standard templates for Galactic diffuse emission model (`gll_iem_v07.fits`) and isotropic diffuse emission (`iso_P8R3_SOURCE_V2_v1.txt`) as used in the fourth *Fermi* catalogue (4FGL; Abdollahi et al. (2020)).

#### 2.1.1 Eleven Years Averaged Spectrum

To calculate the average flux for the 11 years dataset, we begin with an initial automatic optimisation of the ROI by iteratively fitting

the sources using the `optimize` method of *Fermipy*. It is recommended by the *Fermipy* developers to run this method at the start of the analysis “to ensure that all parameters are close to their global likelihood maxima”<sup>2</sup>. After that, both normalisations and spectral parameters of the sources within  $5^\circ$  and only normalisations of the sources lying within  $12^\circ$  of the ROI centre were left to vary. We freeze the spectral parameters for sources having Test Statistic (TS) < 1 or a predicted number of counts (Npred) after initial optimisation less than  $10^{-3}$ . Following Meyer et al. (2019), the normalisations of the Galactic and isotropic diffuse backgrounds, including the spectral index of the Galactic diffuse background template, were left free during the fit. A TS map was generated using `findsource` tool of *Fermipy* to search for additional point sources, that are not present in the 4FGL-DR2 catalogue. No new sources were detected with  $TS \geq 25$ .

The source was modelled using simple power-law

$$\frac{dF}{dE} = N \left( \frac{E}{E_0} \right)^{-\alpha}$$

and log-parabola

$$\frac{dF}{dE} = N \left( \frac{E}{E_b} \right)^{-\alpha - \beta \log \left( \frac{E}{E_b} \right)}$$

models.

Here,  $\frac{dF}{dE}$  and  $N$  are the differential flux and normalisation factor, respectively in the unit of  $\text{photon cm}^{-2}\text{s}^{-1} \text{ MeV}^{-1}$ .  $E$  is the energy,  $E_0$  and  $E_b$  are the scale and break value, respectively in the unit of MeV.  $\alpha$  and  $\beta$  are the spectral parameters. The source was considered to be detected if its  $TS > 25$ , which corresponds to  $\sim 4\sigma$  confidence (Mattox et al. 1996). The source spectrum is considered significantly curved if two times the difference in log-likelihood value for log-parabola and log-likelihood value for power-law ( $TS_{\text{curve}}$ ) is greater than 16 (Acero et al. 2015). The average spectrum of NGC 1275, utilising the 10 years of *Fermi* observations is reported to be significantly curved (Ballet et al. 2020). Utilising the 11 years data set, we also noticed a significant curvature in the source spectrum.

#### 2.1.2 Temporal Analysis

The monthly averaged  $\gamma$ -ray light curves in the energy bands 100 MeV to 100 GeV, 100 MeV to 1 GeV, and 1 GeV to 100 GeV were computed using `lightcurve` tool of *Fermipy*. The best fit model obtained for the 11 years dataset considering a power-law spectrum for NGC 1275 was used as an input model. While constructing the  $\gamma$ -ray lightcurve in 100 MeV to 100 GeV energy band, both normalisations and spectral parameters of the sources within  $3^\circ$  and only normalisations of sources within  $3^\circ$  to  $12^\circ$  from ROI centre were left free to vary in the input model of each time bin. For  $\gamma$ -ray lightcurves in 100 MeV to 1 GeV energy band and 1 GeV to 100 GeV energy band, only normalisations of the sources within  $12^\circ$  from ROI centre were left free to vary in the input model for each time bin. For all the three light curves, the normalisations of the Galactic and isotropic diffuse emission models were left free, and the spectral index of the Galactic emission was frozen to the 11 years averaged value. A signature of increase in the baseline flux was noticed from 2008 to 2017 (Fig 1-a). This was followed by a large, broad flare until 2019.

<sup>1</sup> <https://fermi.gsfc.nasa.gov/ssc/data/analysis/user/>

<sup>2</sup> <https://fermipy.readthedocs.io/en/latest/>

In a previous work, Tanada et al. (2018) studied  $\gamma$ -ray variability of NGC 1275 utilising  $\sim 8$  years of *Fermi* observations (2008 – 2016) and defined two epochs (epoch A: before February 2011 and epoch B: after February 2011) in the light curve based on the variations in the spectral indices. In this work, we have defined different activity states in the monthly averaged  $\gamma$ -ray light curve utilising 11 years of *Fermi* observations based on the increase in the baseline flux nature. To define different states, we calculated the cumulative flux of the monthly averaged  $\gamma$ -ray light curve. A constant slope in cumulative lightcurve corresponds to insignificant variation in flux. Whereas, an increase/decrease in slope indicates a rise/fall in baseline flux. Visual inspection of the cumulative flux distribution suggests the presence of four distinct regions/states. The first three states exhibit linear feature with increase in slopes, whereas, a significant non-linearity was noticed beyond that (state four). To constrain the boundaries of these states, data from shaded regions, as shown in Fig 1-b, were fitted with linear functions. These regions were chosen in a way to avoid edge and/or transition effect. The mid-point of the monthly bin that contains the intersection of the fitted linear functions in the first and the second intervals is considered as the upper boundary of state 1 (S1). Similarly, the mid-point of the monthly bin that contains the intersection of the fitted linear functions in the second and the third intervals is considered as the upper boundary of state 2 (S2). A noticeable deviation from the fitted linear function in interval 3 is considered as the upper boundary of state 3 (S3). Boundaries of these states are indicated in Fig 1-a. Beyond state 3, a significant non-linearity was noticed in the cumulative flux, first a sharp increase followed by a gradual decrease. This region represents the state 4 (S4). The details of the boundaries of these states are mentioned in Table 1. Fig 1-c shows the variation of the monthly averaged spectral parameter  $\alpha$  of this source. The epoch A and epoch B as defined in Tanada et al. (2018) overlap with S1-S2 and S2-S3, respectively.

### 2.1.3 Time-resolved Spectrum

$\gamma$ -ray spectral analysis was carried out in different activity states to study the behaviour of the source. The average flux in the four activity states as defined in the  $\gamma$ -ray light curve was calculated following the methodology used for spectral analysis of the entire data set (Sec. 2.1.1). To calculate the average flux in an activity state, the spectral index of the Galactic diffuse background template was kept frozen to the 11 years averaged value. For all the four states, it was found that the log-parabola spectral model was strongly preferred over the power-law model. The best fit values of spectral parameters are given in Table 1. The spectral parameter  $\alpha$  of the source in all four states lies in the range 2.0 – 2.1. An increase of average  $\gamma$ -ray flux was noticed from S1 to S4.  $\gamma$ -ray SEDs were constructed for 8 logarithmically-spaced energy bins per decade in 100 MeV to 100 GeV energy band using the *sed* tool of *Fermipy* for these four states. The spectral index in each energy bin was frozen to the power-law approximation (local index) to the shape of the global spectrum, while normalisation was left to vary.

*AstroSat* observed NGC 1275 on 2017 January 12-13 under Target of Opportunity (ToO: hereafter referred to as AS1) which falls in the later phase of the S3 state. NGC 1275 was observed again with *AstroSat* on 2017 September 26-27 (referred to as AS2 in the rest of the paper) which falls at the beginning of the S4 state. The  $\gamma$ -ray analysis during AS1 and AS2 was carried out following a similar methodology as used in S1-S4 states. However, due to limited photon statistics, a simple power-law was considered to model the source spectrum during these AS1 and AS2 states. The

normalisations and spectral parameters of sources within  $3^\circ$ , only normalisations of sources within  $3^\circ$  to  $12^\circ$  from ROI centre and, normalisations of the Galactic and isotropic emission were left free to vary. We freeze the normalisations and spectral parameters for sources having  $TS < 1$  or  $N_{pred}$  after initial optimisation less than  $10^{-3}$ . While constructing the  $\gamma$ -ray SED during AS1 and AS2, two energy bins per decade in the full energy band were considered. Due to low photon statistics, the data in the last two energy bands in the  $\gamma$ -ray SED was merged into a single energy band. The flux and spectral parameters during AS1 and AS2 observing periods are given in Table 1. The  $\gamma$ -ray flux during AS1 and AS2 (2 days of observation) is higher than the average flux during the longer duration states (a few years of observation).

## 2.2 X-ray DATA

For X-rays, we used data from the *Swift* X-ray Telescope (*Swift*-XRT; Burrows et al. 2005) that covers the energy range for 0.3 – 10 keV as well as SXT and LAXPC onboard *AstroSat*. The energy ranges of SXT and LAXPC are 0.3 – 8 keV and 3 – 80 keV, respectively.

### 2.2.1 *Swift*-XRT

Though there was no continuous monitoring of this source in the X-ray band, a significant number of pointed observations were carried out by *Swift*-XRT. Fukazawa et al. (2018) analysed archival *Swift*-XRT data of NGC 1275 from 2007-2015. They derived flux for each observation ID and calculated the light curve. In this work, we have calculated the light curve in a similar way utilising all the archival *Swift*-XRT photon counting (PC) mode observations<sup>3</sup> covering S1, S2 and S3 states. Only one observation is present in S1, which is also studied by Fukazawa et al. (2018). There are 16, and 50 PC mode observations present during S2 and S3 state, respectively. The analysis results of 14 and 4 PC mode observations during S2 and S3, respectively were given in Fukazawa et al. (2018). During the AS1 state, there are no *Swift*-XRT PC mode observations available. However, one *Swift*-XRT observation in windowed timing (WT) mode (Obs ID: 00031770015, exposure time:  $\sim 239$  s) was present during this period, which was used in this work. We processed the XRT data using the *xrtDas* (v 3.4.1) package distributed under *HEASOFT* (v 6.24). The task *xrtPipeline* (v 0.13.4) was used to clean and calibrate level 1 data files with standard filtering criteria<sup>4</sup> and using calibration files *CALDB* (v 20190910). The source spectrum was binned to have 20 counts per bin using *GRPPHA*. The XRT spectra were fitted in *XSPEC* version: 12.10.0c (Arnaud 1996).

For PC mode data, the source spectrum was derived considering an annular region from  $12'' - 26''$ . The central  $12''$  region is blocked since the PC mode data suffers from pile-up events. Background spectra were extracted in  $60'' - 65''$  from the centre to account for the cluster emission. Considering the significant difference in the response functions of PC mode and WT mode of *Swift*-XRT below 1.6 keV (Godet et al. 2009), following Fukazawa et al. (2018), we restricted our analysis to 1.6 – 10.0 keV energy band. The XRT spectra were fitted with model “phabs”, single temperature “apec” and power-law to account for Galactic absorption, the emission from hot gas in the Perseus cluster and the AGN emission,

<sup>3</sup> <https://heasarc.gsfc.nasa.gov/cgi-bin/W3Browse/w3browse.pl>

<sup>4</sup> [https://swift.gsfc.nasa.gov/analysis/xrt\\_swguide\\_v1\\_2.pdf](https://swift.gsfc.nasa.gov/analysis/xrt_swguide_v1_2.pdf)

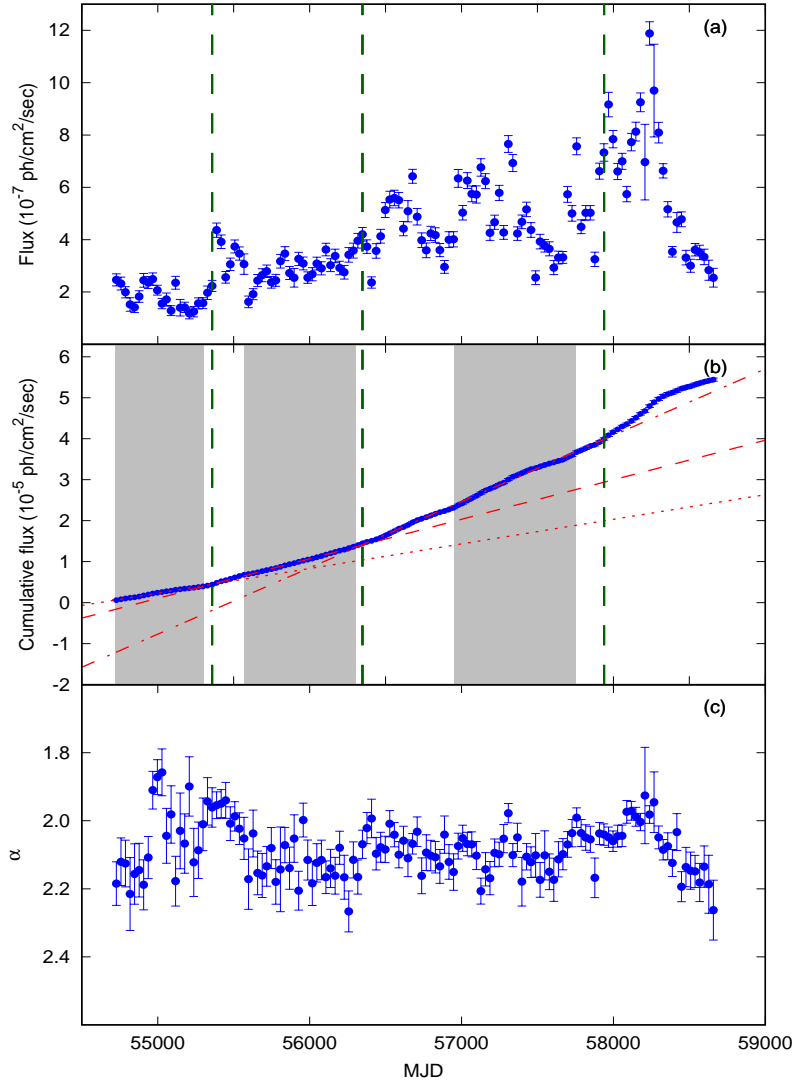


**Figure 1.** (a): Monthly averaged  $\gamma$ -ray light curve (100 MeV-100 GeV) for NGC 1275 utilising 11 years of *Fermi* observation (2008-2019). (b): Plot of cumulative flux with time. Data in shaded regions was considered for fitting linear function. The best fit linear functions in the three shaded regions are represented by the dotted line (slope:  $6.0 \times 10^{-9}$  ph/cm<sup>2</sup>/sec/day), dashed line (slope:  $9.6 \times 10^{-9}$  ph/cm<sup>2</sup>/sec/day) and dash-dotted (slope:  $1.6 \times 10^{-8}$  ph/cm<sup>2</sup>/sec/day) line respectively. The vertical lines in (a) and (b) define the boundary of the different states. (c) Variation of the monthly averaged spectral parameter  $\alpha$  for NGC 1275 utilising 11 years of *Fermi* observation (2008-2019).

**Table 1.**  $\gamma$ -ray flux and spectral indices for different activity states

Interval	Start Date MJD	End Date MJD	Flux ( $\times 10^{-7}$ ) ph/cm <sup>2</sup> /sec	alpha	beta	TS <sub>curve</sub>
(1)	(2)	(3)	(4)	(5)	(6)	(7)
State 1 (S1)	2008 Aug 05 (54683)	2010 June 11 (55358)	$1.72 \pm 0.07$	$2.02 \pm 0.02$	$0.04 \pm 0.01$	19.3
State 2 (S2)	2010 June 11 (55358)	2013 Feb 25 (56348)	$2.74 \pm 0.08$	$2.07 \pm 0.01$	$0.060 \pm 0.007$	79.4
State 3 (S3)	2013 Feb 25 (56348)	2017 July 04 (57938)	$4.44 \pm 0.06$	$2.069 \pm 0.008$	$0.059 \pm 0.005$	212.9
State 4 (S4)	2017 July 04 (57938)	2019 Aug 05 (58700)	$5.01 \pm 0.18$	$2.02 \pm 0.02$	$0.07 \pm 0.01$	129.8
AS1	2017 Jan 12 (57765)	2017 Jan 14 (57767)	$8.6 \pm 1.5$	$2.0 \pm 0.1$	-	3.4
AS2	2017 Sep 26 (58022)	2017 Sep 28 (58024)	$5.4 \pm 1.6$	$2.1 \pm 0.2$	-	0.002



respectively. The Galactic hydrogen column density ( $N_H$ ) frozen to  $1.5 \times 10^{21} \text{ cm}^{-2}$  (Yamazaki et al. 2013; Tanada et al. 2018). We fix the temperature and abundance of the “apec” model to 4.1 keV and 0.65 solar, respectively (Fukazawa et al. 2018) and estimate the normalisation of the “apec” model in each observation. The “apec” normalisation was then frozen to the median value of 0.0099<sup>5</sup>, and the AGN flux and photon index was derived in each observation ID. AGN flux was derived using “cflux” routine in XSPEC. No significant variation in photon indices was noticed during S2 and S3 states. The source flux exhibits noticeable variations in both S2 and S3 states with a fractional variance of  $23\% \pm 7\%$  and  $29\% \pm 4\%$ , respectively. Since our prime objective is to study the average source properties during these states, we used the flux and photon indices from each ID to calculate the average flux and photon indices during S2 and S3 states. The flux and photon index values in each of these individual observation IDs are summarised in Table 2. Fig. 2 and Fig. 3 represents the flux and photon index values in each ID during S2 and S3 respectively, where the horizontal solid lines and dashed lines represent the weighted mean and error in weighted mean, respectively. The cases where power-law parameters could not be constrained are not considered while calculating the weighted mean and are also not shown in Table 2, Fig. 2 and Fig. 3. The values of average flux and photon indices are given in Table 3. Similar to  $\gamma$ -rays, a signature of average flux enhancement without any significant change in the photon index from S1 to S3 was observed.

The WT mode data during the AS1 period was analysed following the methodology described in Fukazawa et al. (2018). The spectra was extracted within  $0.3'$  of NGC 1275. The corresponding extraction region is  $36 \times 1416 \text{ arcsec}^2$  in the sky. All the PC mode data was used to extract the background spectra from the same sky region as that of WT mode spectra after excluding the central  $36 \times 36 \text{ arcsec}^2$ , and subtracted from the WT mode spectra. A 3% systematic error was considered during the spectral analysis of WT mode data. Parameters of the “apec” model namely, temperature, abundance, and normalisation were fixed to 4.0 keV, 0.60 solar and 0.0208, respectively (Fukazawa et al. 2018). The best fit values of flux and photon index are given in Table 3. Recently, Imazato et al. (2021) have presented *Swift*-XRT light curves of NGC 1275. From visual inspection of their light curves, for the data in common, we found good agreement between our results and that of Imazato et al. (2021).

### 2.2.2 *AstroSat*

The Level 1 SXT data was analysed using “SXTPIPELINE” of the SXT software “as1sxtlevel2-1.4b”. The clean events were merged using the “sxtpyjuliameger\_v01”. A circular region of  $15'$  radius was used as a source region, and for the background, the instrument team provided “*SkyBkg\_comb\_EL3p5\_Cl\_Rd16p0\_v01.pha*” file was used. The ancillary response file was created by using “sxteeefmodule\_v02”. A 2% systematic error was considered during spectral analysis.

LAXPC data was analysed using the analysis software “LAXPC\_SOFT” package (May 19, 2018 version) available at the *AstroSat* Science Support Cell<sup>6</sup>. Standard procedures were used

to reduce the Level 1 data (Yadav et al. 2016a; Antia et al. 2017). The spectra for the source and background in the energy range of 4.0 – 13.0 keV were created using the layer 1 data of PCU unit 20. The energy resolution of LAXPC is 15%. Therefore, it is recommended by the LAXPC instrument team that the spectrum should be re-binned such that the energy bin width is at least 5% of the central energy (energy grouping factor 0.05). Hence, in our analysis, we considered a value of 0.05 for energy grouping factor. Since the size of the emission region is large, the systematic error of LAXPC is expected to be high. We considered a 3% systematic error for LAXPC spectral analysis.

Due to the large source extraction region of *AstroSat*-SXT ( $\sim 15'$  radius) and *AstroSat*-LAXPC ( $1^\circ \times 1^\circ$  field of view), the observed X-ray flux of NGC 1275 suffers significant contamination from the Perseus cluster. Therefore, to obtain intrinsic emission from the nucleus of NGC 1275, it is essential to constrain cluster parameters. For SXT and LAXPC analysis, the cluster abundance was frozen to the value of 0.42 solar, which was obtained by averaging the data from Fig. 6 of Churazov et al. (2003) over a region of  $15'$  radius. This value of abundance is consistent with other studies (Schmidt et al. 2002; Nishino et al. 2010). The temperature and abundance of the “apec” model, were constrained utilising simultaneous *Swift*-XRT observation.

As during *Swift*-XRT analysis data below 1.6 keV was not considered; we restricted our SXT data analysis to 1.6 – 7.0 keV energy band. For SXT analysis during the AS1 observing period (exposure time  $\sim 33$  ks), the photon index and the unabsorbed flux of the power-law component were kept frozen to the values derived from the simultaneous *Swift*-XRT observation to estimate the temperature ( $5.60 \pm 0.09$  keV) and normalisation ( $0.708 \pm 0.003$ ) of the “apec” model. For SXT analysis during the AS2 observing period (exposure time  $\sim 17$  ks), the temperature and normalisation were kept frozen to the best fit values obtained during the AS1 observing period, and the unabsorbed flux from NGC 1275 was obtained (Table 4).

During LAXPC analysis in the AS1 period (exposure time  $\sim 50$  ks), the photon index and the unabsorbed flux of the power-law component (emission from NGC 1275) were kept frozen to the values derived from simultaneous *Swift*-XRT observation in 4.0–13.0 keV energy range and the best fit values of the temperature ( $5.9 \pm 0.1$  keV) and normalisation ( $0.75 \pm 0.02$ ) of the “apec” model were obtained. During the AS2 observing period (exposure time  $\sim 16$  ks), the “apec” temperature and normalisation were kept frozen to the values obtained during the AS1 period. Due to low photon statistics, the photon index of the source could not be constrained with LAXPC observation. Therefore, the power-law photon index was kept frozen to the best fit value obtained during simultaneous SXT observation. The unabsorbed flux from NGC 1275 in 4.0–13.0 keV energy band is given in Table 4.

<sup>5</sup> The “apec” normalisation, in units of  $\frac{10^{-14}}{4\pi[D_A(1+z)]^2} \int n_e n_H dV$ , where  $D_A$  is the angular diameter distance to the source in cm,  $n_e$  and  $n_H$  are the electron and Hydrogen densities in  $\text{cm}^{-3}$ , respectively (followed throughout the paper).

<sup>6</sup> [http://astrosat-ssc.iucaa.in/?q=data\\_and\\_analysis](http://astrosat-ssc.iucaa.in/?q=data_and_analysis)

Table 2: Summary of *Swift*-XRT PC mode observations . ★ marks the observation IDs analysed by [Fukazawa et al. \(2018\)](#).

State	Sequence No.	Date	Exposure Time (seconds)	Flux (in $\times 10^{-11}$ erg/cm <sup>2</sup> /sec)	Photon index
S1	00030354003*	2009-12-30 (55195)	4328	$1.7 \pm 0.4$	$1.9 \pm 0.5$
S2	00031770001*	2010-07-22 (55399)	2198	$2.9 \pm 0.5$	$2.1^{+0.4}_{-0.3}$
	00031770002*	2010-07-24 (55401)	2048	$4.1 \pm 0.7$	$1.8 \pm 0.3$
	00031770003*	2010-07-26 (55403)	2045	$2.0 \pm 0.4$	$3.0^{+0.6}_{-0.5}$
	00031770004*	2010-07-28 (55405)	2183	$3.2 \pm 0.6$	$1.8 \pm 0.4$
	00031770005	2010-07-30 (55407)	2125	$1.7 \pm 0.4$	$3.1^{+0.6}_{-0.5}$
	00031770006*	2010-08-01 (55409)	2119	$2.6^{+0.8}_{-0.7}$	$1.2^{+0.5}_{-0.6}$
	00031770007*	2010-08-03 (55411)	2412	$3.3 \pm 0.6$	$1.4 \pm 0.4$
	00031770008*	2010-08-05 (55413)	1998	$2.3^{+0.8}_{-0.7}$	$1.9 \pm 0.7$
	00031770009*	2010-08-07 (55415)	2113	$3.9 \pm 0.6$	$1.7 \pm 0.3$
	00031770010*	2010-08-09 (55417)	2118	$3.7^{+0.7}_{-0.6}$	$1.5 \pm 0.3$
	00091128002*	2011-07-06 (55748)	1349	$3.2^{+0.9}_{-0.8}$	$1.6 \pm 0.5$
	00091128003*	2011-07-07 (55749)	1771	$1.4^{+0.5}_{-0.4}$	$2.8^{+0.8}_{-0.6}$
	00091128004*	2011-07-09 (55751)	3479	$2.3^{+0.7}_{-0.6}$	$1.1^{+0.5}_{-0.6}$
	00091128005*	2011-07-10 (55752)	4925	$1.7 \pm 0.4$	$1.8 \pm 0.4$
S3	00049799004*	2013-07-14 (56487)	5282	$3.3 \pm 0.4$	$1.6 \pm 0.2$
	00049799005*	2013-07-26 (56499)	3077	$2.9 \pm 0.5$	$1.8 \pm 0.3$
	00049799006*	2013-08-01 (56505)	1573	$3.1^{+1.0}_{-0.8}$	$1.4 \pm 0.6$
	00092034001	2015-02-11 (57064)	2003	$3.4 \pm 0.5$	$2.7^{+0.4}_{-0.3}$
	00092034002*	2015-03-15 (57096)	2150	$3.4^{+0.7}_{-0.6}$	$1.6^{+0.4}_{-0.3}$
	00092034003	2015-07-25 (57228)	2005	$4.0 \pm 0.6$	$1.7 \pm 0.3$
	00092034004	2015-08-18 (57252)	2008	$2.9^{+0.9}_{-0.8}$	$1.8^{+0.7}_{-0.6}$
	00081530001	2015-11-03 (57329)	6428	$2.3 \pm 0.3$	$2.2 \pm 0.3$
	00034380001	2016-02-19 (57437)	2475	$3.2 \pm 0.5$	$1.9 \pm 0.3$
	00034380002	2016-02-21 (57439)	2480	$3.1 \pm 0.5$	$2.4 \pm 0.3$
	00034380004	2016-02-23 (57441)	2417	$2.2 \pm 0.5$	$1.7 \pm 0.5$
	00034380005	2016-02-25 (57443)	2757	$2.3^{+0.6}_{-0.5}$	$1.5^{+0.4}_{-0.5}$
	00034380006	2016-02-26 (57444)	2780	$2.6 \pm 0.5$	$2.2^{+0.4}_{-0.3}$
	00034380007	2016-02-29 (57447)	1703	$3.1^{+0.8}_{-0.7}$	$1.7^{+0.5}_{-0.4}$
	00034380008	2016-03-02 (57449)	2382	$1.6^{+0.5}_{-0.4}$	$3.2^{+0.9}_{-0.6}$
	00034380010	2016-03-03 (57450)	2030	$3.4^{+0.6}_{-0.5}$	$2.2 \pm 0.3$
	00034404001	2016-03-05 (57452)	3976	$2.2 \pm 0.5$	$1.8 \pm 0.4$
	00034380012	2016-03-06 (57453)	2362	$3.5^{+0.6}_{-0.5}$	$1.7 \pm 0.3$
	00034380013	2016-03-08 (57455)	2914	$1.7^{+0.5}_{-0.4}$	$2.4^{+0.6}_{-0.5}$
	00034380014	2016-03-10 (57457)	2240	$3.3^{+0.6}_{-0.5}$	$1.9 \pm 0.3$
	00034380015	2016-03-12 (57459)	2285	$3.2 \pm 0.5$	$2.1 \pm 0.3$
	00034404003	2016-03-16 (57463)	2185	$3.0^{+0.8}_{-0.7}$	$1.2^{+0.5}_{-0.6}$
	00034765001	2016-10-30 (57691)	1973	$3.3^{+0.7}_{-0.6}$	$2.1 \pm 0.4$
	00034765002	2016-10-31 (57692)	1983	$3.4^{+0.6}_{-0.5}$	$2.1 \pm 0.3$
	00034765003	2016-11-01 (57693)	1878	$5.6 \pm 0.8$	$1.5 \pm 0.3$
	00034765005	2016-11-03 (57695)	1611	$1.4^{+0.7}_{-0.5}$	$3.0^{+1.1}_{-0.8}$
	00034765006	2016-11-04 (57696)	1696	$3.8^{+1.4}_{-1.1}$	$1.3 \pm 0.6$
	00034765007	2016-11-05 (57697)	1808	$4.0^{+0.6}_{-0.5}$	$2.4 \pm 0.3$
	00034765008	2016-11-06 (57698)	2010	$2.6^{+0.8}_{-0.7}$	$1.4 \pm 0.5$
	00034765009	2016-11-07 (57699)	1958	$4.2^{+0.7}_{-0.6}$	$2.0 \pm 0.3$
	00034765010	2016-11-08 (57700)	1613	$6.7^{+0.9}_{-0.8}$	$1.4 \pm 0.2$
	00034765011	2016-11-09 (57701)	1543	$4.1 \pm 0.9$	$1.5 \pm 0.4$
	00034765012	2016-11-10 (57702)	1935	$3.2 \pm 0.6$	$1.9 \pm 0.4$
	00087312001	2016-12-31 (57753)	956	$3.7^{+0.9}_{-0.8}$	$2.7 \pm 0.5$
	00087311001	2017-01-01 (57754)	634	$6.8 \pm 1.2$	$2.3 \pm 0.4$
	00087311002	2017-01-02 (57755)	797	$6.1 \pm 1.0$	$2.1 \pm 0.3$
	00087311003	2017-03-15 (57827)	1079	$4.5^{+1.0}_{-0.8}$	$2.2 \pm 0.4$
	00087312002	2017-03-21 (57833)	1466	$2.9 \pm 0.6$	$2.5^{+0.5}_{-0.4}$
	00087311005	2017-03-24 (57836)	2420	$2.8^{+0.6}_{-0.5}$	$1.5 \pm 0.4$
	00087312004	2017-03-26 (57838)	4797	$2.7 \pm 0.3$	$2.0 \pm 0.2$
	00087312005	2017-03-31 (57843)	2143	$4.2^{+0.8}_{-0.7}$	$1.5^{+0.3}_{-0.4}$

**Table 3.** *Swift*-XRT analysis results for different activity states

Activity state	$F_{1.6-10.0 \text{ keV}}^a$	$\Gamma_{1.6-10.0 \text{ keV}}^b$
State 1	$1.7 \pm 0.4$	$1.9 \pm 0.5$
State 2	$2.4 \pm 0.1$	$1.8 \pm 0.1$
State 3	$3.02 \pm 0.09$	$1.90 \pm 0.05$
AS1	$1.8^{+0.9}_{-0.7}$	$1.9^{+0.9}_{-0.8}$

<sup>a</sup> 1.6-10.0 keV unabsorbed flux in units of  $10^{-11} \text{ erg cm}^{-2} \text{ s}^{-1}$ <sup>b</sup> 1.6-10.0 keV photon index of power-law model**Table 4.** *AstroSat*-SXT and LAXPC analysis results during AS2 period

Instrument	Energy range (keV)	$F^a$	$\Gamma^b$	$\chi^2/\text{dof}$
SXT	1.6 – 7.0	$3.0 \pm 0.3$	$2.7 \pm 0.3$	496.89/439
LAXPC	4.0 – 13.0	$0.6 \pm 0.4$	$2.7^c$	9.64/13

<sup>a</sup> Unabsorbed flux in units of  $10^{-11} \text{ erg cm}^{-2} \text{ s}^{-1}$ <sup>b</sup> Photon index of power-law model<sup>c</sup> Photon index kept frozen to the best fit value obtained during simultaneous SXT observation.**Table 5.** *Swift*-UVOT flux values in different UVOT filters for different activity states

Filters	S1 <sup>a</sup>	S2 <sup>a</sup>	S3 <sup>a</sup>	AS1 <sup>a</sup>
V	–	$10.5 \pm 0.3$	$13.2 \pm 0.4$	–
B	–	$7.4 \pm 0.3$	$9.1 \pm 0.3$	–
U	–	$4.3 \pm 0.2$	$6.2 \pm 0.2$	–
UVW1	$1.9 \pm 0.1$	$2.9 \pm 0.2$	$3.9 \pm 0.2$	–
UVM2	–	$3.0 \pm 0.1$	$3.6 \pm 0.2$	–
UVW2	–	$2.3 \pm 0.1$	$2.9 \pm 0.2$	$3.4 \pm 0.2$

<sup>a</sup> Flux in units of  $10^{-26} \text{ erg cm}^{-2} \text{ s}^{-1} \text{ Hz}^{-1}$ **Table 6.** *AstroSat*-UVIT analysis results

Filter	$\lambda_{\text{mean}}(\text{\AA})$	Flux <sup>a</sup>
CaF2-1 (F1)	1481	$2.21 \pm 0.02$
Silica (F5)	1717	$3.06 \pm 0.04$
NUVB15 (F2)	2196	$4.83 \pm 0.05$
NUVB4 (F5)	2632	$4.32 \pm 0.03$

<sup>a</sup> Flux in  $10^{-26} \text{ erg cm}^{-2} \text{ s}^{-1} \text{ Hz}^{-1}$ 

### 2.3 UV/Optical data

For data in the UV/optical bands, we used both *Swift*-UVOT (Romíng et al. 2005) and UVIT onboard *AstroSat*. From *Swift*-UVOT, we have observations in U, B, V, UVW1, UVW2, and UVM2 filters for different activity states. The level 2 products<sup>7</sup> were analysed using different tasks, which are a part of HEASOFT (v 6.24), and 20170922 version of CALDB. UVOTIMSUM task was used to merge the different observations during a particular epoch.

For photometry, a source region with radius  $\sim$  point spread function was chosen to reduce cluster/host galaxy contribution. A circular source region with  $3''$  radius centred at the source position and an annular background region with inner and outer radii of  $15''$

and  $20''$  was used. UVOTSOURCE task was used to get the source magnitude. The Galactic extinction was calculated using Cardelli et al. (1989) and Schlafly & Finkbeiner (2011). The extinction corrected AB magnitudes were then converted to flux ( $\text{erg cm}^{-2} \text{ s}^{-1}$ ). During S2 and S3 states, the source was observed in all the *Swift*-UVOT filters. In the state S2, the exposure times for V, B, U, UVW1, UVM2 and UVW2 filters are  $\sim 3 \text{ ks}$ ,  $\sim 3 \text{ ks}$ ,  $\sim 6 \text{ ks}$ ,  $\sim 11 \text{ ks}$ ,  $\sim 8 \text{ ks}$  and  $\sim 17 \text{ ks}$ , respectively. For the state 3, the exposure times for V, B, U, UVW1, UVM2 and UVW2 filters are  $\sim 5 \text{ ks}$ ,  $\sim 5 \text{ ks}$ ,  $\sim 23 \text{ ks}$ ,  $\sim 33 \text{ ks}$ ,  $\sim 23 \text{ ks}$ ,  $\sim 30 \text{ ks}$  seconds respectively. However, during S1 and AS1 states, the source was only observed in UVW1 (exposure time:  $\sim 4 \text{ ks}$ ) and UVW2 filters (exposure time: 232 seconds), respectively. The Galactic extinction corrected fluxes in different UVOT filters during S1, S2, S3 and AS1 observing periods are given in Table 5. *Swift*-UVOT light curves of NGC 1275 were recently presented by Imazato et al. (2021). As they have corrected for the host galaxy contribution to the observed UV/optical emission, it is likely that the flux values quoted in Table 5 are marginally brighter than that of Imazato et al. (2021).

Similar to the X-ray and  $\gamma$ -ray bands, an increase in the average source flux was noticed from S1 to S3. Utilising the fluxes obtained in three optical and three UV filters and considering a power-law spectral shape, averaged energy spectral indices of optical and UV fluxes were derived in S2 and S3 states. An energy spectral index of  $1.9 \pm 0.3$  and  $1.65 \pm 0.01$  was obtained in the optical band for the S2 and S3 states respectively. Similarly, in the UV band, energy spectral index of  $1.1 \pm 0.8$  and  $1.2 \pm 0.4$  was obtained for the S2 and S3 states respectively. Hence, no appreciable change in spectral indices was noticed in these states.

NGC 1275 was observed with *AstroSat*-UVIT under AS2 observation in FUV filters: CaF2-1 (exposure time  $\sim 4 \text{ ks}$ ) and Silica (exposure time  $\sim 8 \text{ ks}$ ) and NUV filters: NUVB15 (exposure time  $\sim 8 \text{ ks}$ ) and NUVB4 (exposure time  $\sim 4 \text{ ks}$ ). The science ready visual aspect corrected Level-2 images provided by Indian Space Science Data Centre (ISSDC) (processed by the pipeline version 6.3) was used to carry out standard photometry using IRAF<sup>8</sup>. A circular aperture of 5 pixels ( $\sim 2.0''$ ) and background region of 15 – 20 pixels ( $\sim 6.0'' - \sim 8.0''$ ) was used for photometry. The derived magnitudes were converted into fluxes (Tandon et al. 2017) and corrected for Galactic extinction. The estimated flux was corrected for the chosen aperture size using Table 11 of Tandon et al. (2020). The Galactic extinction corrected fluxes in four UVIT filters during AS2 observing period are given in Table 6.

## 3 DISCUSSION

### 3.1 Temporal Behaviour

Similar to the long-term variability as observed in blazars (e.g., Bhattacharya et al. 2013, 2017, 2021), Abdo et al. (2009) noticed that the  $\gamma$ -ray flux observed during the first few months of *Fermi* observations was nearly a factor of ten higher than the EGRET flux upper limit suggesting a presence of flux variability of a much longer timescale in NGC 1275. Dutson et al. (2014) reported the presence of a decade timescale variability in this source. Based on the first year of *Fermi* observations of NGC 1275, Kataoka et al.

<sup>7</sup> <https://heasarc.gsfc.nasa.gov/cgi-bin/W3Browse/w3browse.pl>

<sup>8</sup> IRAF is distributed by the National Optical Astronomy Observatory, which is operated by the Association of Universities for Research in Astronomy (AURA) under a cooperative agreement with the National Science Foundation

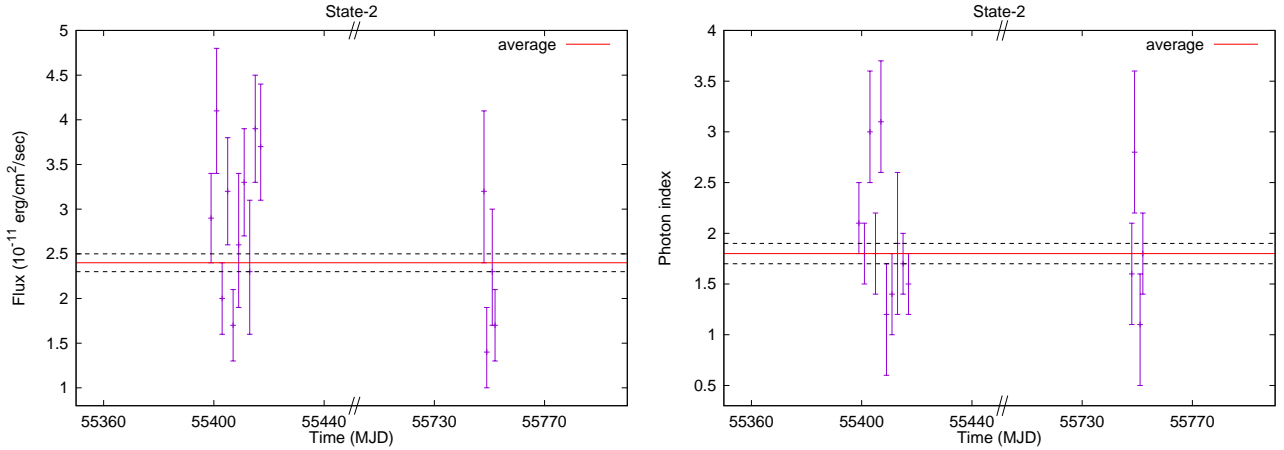


**Figure 2.** *Swift*-XRT light curve and variation of photon index for NGC 1275 for state 2. Left panel: Variation in 1.6 – 10 keV flux. Right panel: Variation in photon index. The solid horizontal lines in both plots represent the weighted average and dashed horizontal lines represent the error in weighted average.

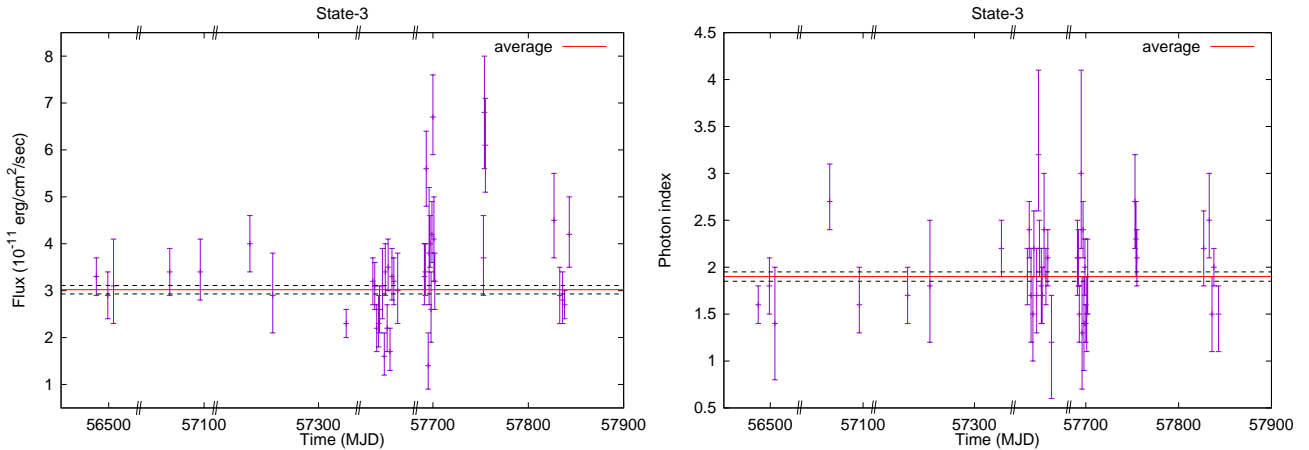


**Figure 3.** *Swift*-XRT light curve and variation of photon index for NGC 1275 for state 3. Left panel: Variation in 1.6 – 10 keV flux. Right panel: Variation in photon index. The solid horizontal lines in both plots represent the weighted average and dashed horizontal lines represent the error in weighted average.

(2010) noticed a monthly timescale variability of the flux and the spectral indices. Short-term variability on hours and sub-week timescales was also noticed in this source (Baghmanyan et al. 2017; Brown & Adams 2011). The hour-timescale variability reported by Baghmanyan et al. (2017) suggests an extremely compact emitting region. Short term ( $\sim$  hours) variability in the optical band was also noticed in a few other  $\gamma$ -ray detected misaligned active galaxies (Bhattacharya et al. 2019).

Tanada et al. (2018) studied the  $\gamma$ -ray variability of NGC 1275 utilising  $\sim 8$  years of *Fermi* observations and defined two epochs (epoch A and epoch B) in the light curve based on the fluctuations in the spectral indices. In the present study, we have defined 4 activity states based on the increase in the baseline flux nature noticed in the monthly averaged  $\gamma$ -ray light curve of NGC 1275 as described in Section 2.1.2. As represented in the top panels of Fig. 4, no significant correlation was noticed between the monthly averaged  $\gamma$ -ray flux and the spectral parameter  $\alpha$  during S1, S2, and S3 states with Pearson correlation coefficient value 0.3,  $-0.2$ , and  $-0.3$  respectively. However, during S4 state, a hint of “flatter when brighter” feature was noticed with a correlation coefficient of  $\sim -0.8$ .

The hardness ratio of this source was also calculated in each

monthly bin utilising the monthly averaged  $\gamma$ -ray fluxes in 100 MeV - 1 GeV and 1 GeV - 100 GeV energy bands, which is represented in bottom panels of Fig. 4. Similar to the findings of the flux-spectral parameter correlation study, no significant correlation was noticed between the flux and the hardness ratio values during S1, S2, and S3 states with the Pearson correlation coefficient value  $-0.3$ ,  $0.1$ , and  $0.2$ , respectively. However, a significant correlation was found during S4 with Pearson correlation coefficient  $0.6$ , supporting a ‘harder when brighter’ scenario. Tanada et al. (2018) found a correlation between the  $\gamma$ -ray flux and the hardness ratio during one of the flares in epoch A of their study. However, in epoch B of their study, which overlaps with S2 and S3 states of this work, no significant correlation was noticed.

A strong positive correlation between the optical and the  $\gamma$ -ray fluxes was noticed by Aleksić et al. (2014) between October 2009 to February 2011. Fukazawa et al. (2018) reported the first positive correlation between fluxes in the X-ray and the  $\gamma$ -ray energy bands during 2013 – 2015. In this work, we noticed a correlated increase of  $\gamma$ -ray, X-ray and UV/optical fluxes averaged over S1, S2 and S3 states without any appreciable change in the spectral indices.



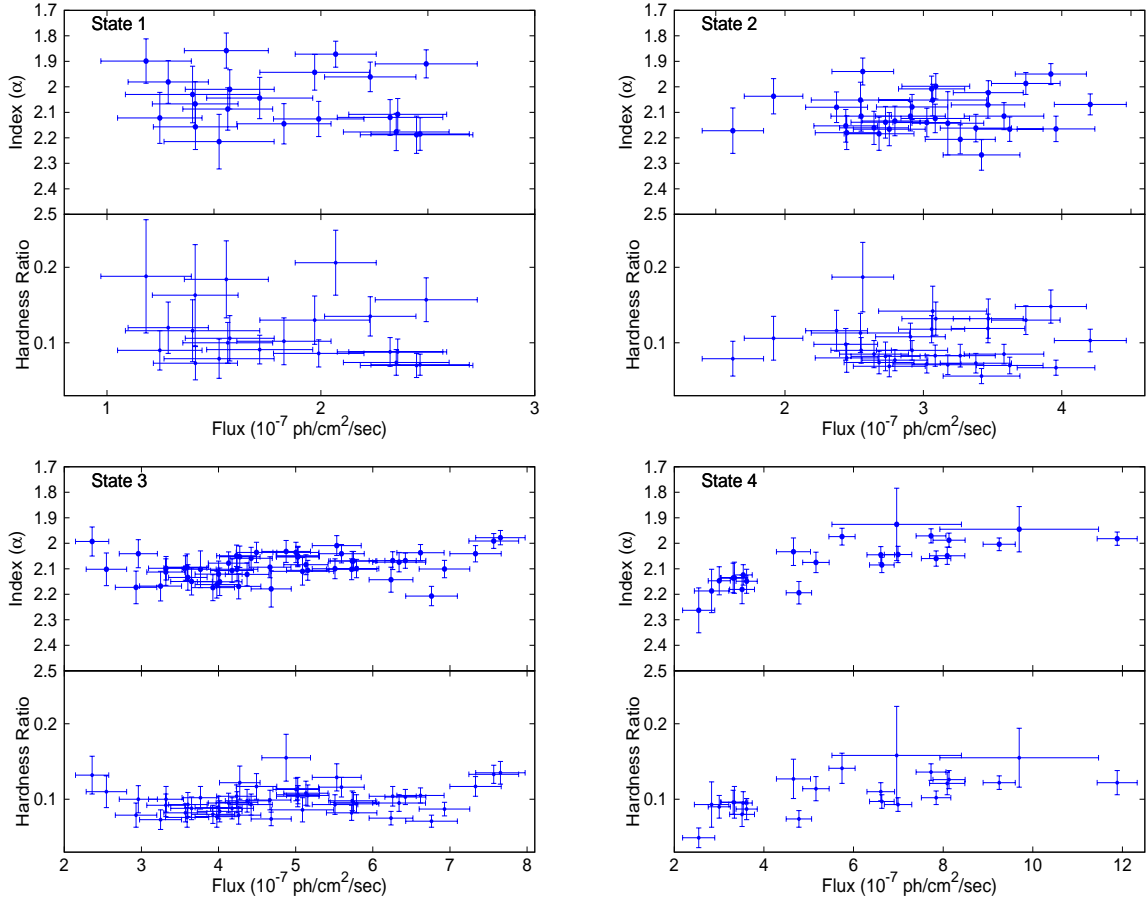


**Figure 4.** Variation of monthly averaged  $\gamma$ -ray flux with photon index (top panel in each sub-figure) and monthly averaged  $\gamma$ -ray flux with hardness ratio (bottom panel in each sub-figure) for the four states identified in the  $\gamma$ -ray light curve.

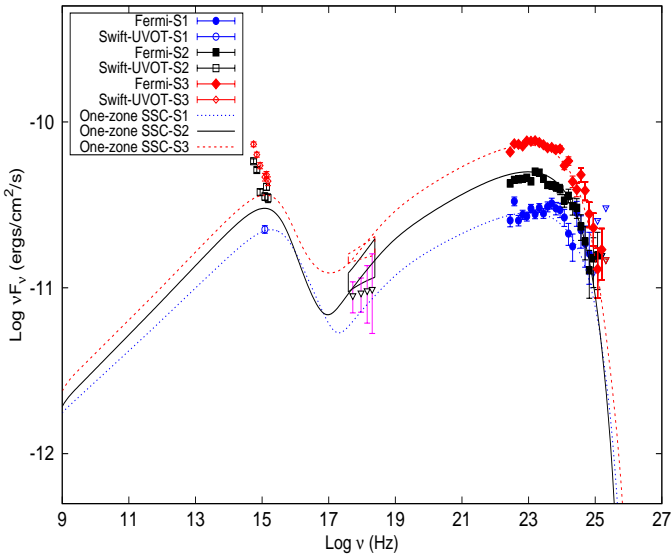


**Figure 5.** SED of NGC 1275 during different activity states. The dotted, solid and dashed lines represents the total (Sync+SSC) SED model contribution from S1, S2, and S3 respectively. The bow-ties in X-ray band for S1, S2, and S3 are from *Swift*-XRT. The downward triangles are for upper limit values.

### 3.2 Modelling of Spectral Energy Distribution

Usually one zone synchrotron self Compton (SSC) jet model has been used to explain the broadband SEDs of NGC 1275 (e.g., [Abdo et al. 2009](#); [Kataoka et al. 2010](#); [Aleksić et al. 2014](#); [Tanada et al. 2018](#)). However, [Tavecchio & Ghisellini \(2014\)](#) considered a “spine-layer” scenario to explain the broadband SED of this source during the MAGIC campaign ([Aleksić et al. 2014](#)).

From the broadband SED modelling of the  $\gamma$ -ray flaring and quiescent states of NGC 1275, [Tanada et al. \(2018\)](#) suggested that flux changes in epoch A were caused by the injection of the high-energy electrons in the jet, while a change of Doppler factor could explain the observed flux variations in epoch B. [Aleksić et al. \(2014\)](#) derived the parameters, which are in the typical range found for BL Lacs (except for bulk Lorentz factor), from the broadband SED modelling of simultaneous observations in two campaigns (October 2009–February 2010 and August 2010–February 2011) of NGC 1275. They suggested that NGC 1275 could be a misaligned BL Lac with large jet inclination angle and small bulk Lorentz factor. Alternatively, it might be more aligned with smaller jet inclination angle and higher bulk Lorentz factor.

In the present work, we have studied the average behaviour of the source at its various activity states. Broadband SEDs of the source were constructed and modelled during S1, S2 and S3 states. Due to the lack of adequate multi-band data, averaged broadband SED study could not be carried out during the S4 state. We also constructed and modelled the broadband SEDs during AS1 and AS2

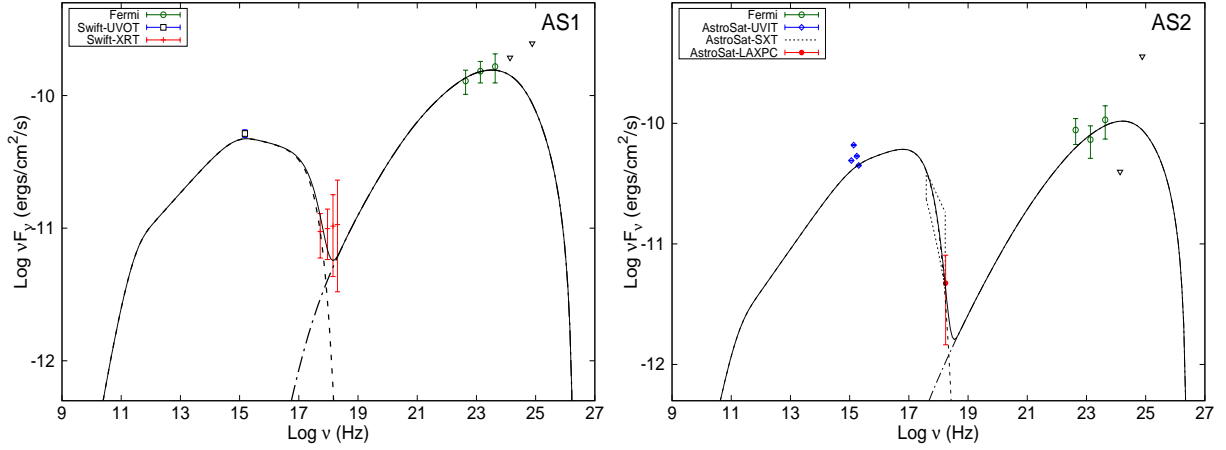


**Figure 6.** SED of NGC 1275 during *AstroSat* observing periods. The dashed line represents the contribution from synchrotron emission and dash-dotted line represents the contribution from SSC emission. The solid line represents the total (Sync+SSC) SED model contribution. The downward triangles are for upper limit values.

**Table 7.** Model parameters for the SED

Parameter	Symbol	State 1	State 2	State 3	<i>AstroSat</i> -AS1	<i>AstroSat</i> -AS2
Minimum electron Lorentz factor	$\gamma_1$	15.0	19.0	20.0	450	350
Maximum electron Lorentz factor	$\gamma_2$	$2.6 \times 10^5$	$2.0 \times 10^5$	$4.0 \times 10^5$	$5.7 \times 10^5$	$7.1 \times 10^5$
Break Lorentz factor	$\gamma_b$	$6.0 \times 10^4$	$5.0 \times 10^4$	$5.0 \times 10^4$	$3.0 \times 10^4$	$4.0 \times 10^4$
Normalisation of particle spectrum	$N_0$	$3.25 \times 10^{44}$	$7.93 \times 10^{44}$	$9.31 \times 10^{44}$	$4.90 \times 10^{45}$	$1.81 \times 10^{45}$
Particle spectral index (before break)	$p_1$	2.6	2.6	2.6	2.5	2.3
Particle spectral index (after break)	$p_2$	4.1	4.5	4.4	3.1	2.8

states. During AS1, data from UVW2 filter of *Swift*-UVOT, *Swift*-XRT and *Fermi*-LAT were used to model the broadband SED. During AS2, data from four filters of *AstroSat*-UVIT, *AstroSat*-SXT, *AstroSat*-LAXPC and *Fermi*-LAT were used to model the broadband SED. We considered a single zone leptonic model that includes synchrotron and SSC emission by non-thermal relativistic electrons in relativistically moving emission region (blob) in AGN jet, as described in [Bhattacharyya et al. \(2018\)](#). The energy distribution of relativistic jet electrons was considered as a broken power-law, which is given by

$$\begin{aligned}
 N(\gamma) &= N_0 \left( \frac{\gamma}{\gamma_b} \right)^{-p_1} & \text{for } \gamma_1 \leq \gamma \leq \gamma_b \\
 &= N_0 \left( \frac{\gamma}{\gamma_b} \right)^{-p_2} & \text{for } \gamma_b \leq \gamma \leq \gamma_2
 \end{aligned}$$

where,  $\gamma_1$ ,  $\gamma_2$ , and  $\gamma_b$  are minimum, maximum and break Lorentz factors whereas  $p_1$  and  $p_2$  are the particle spectral indices before and after the break Lorentz factor.

For modelling of SEDs in all the activity states, the employed jet inclination angle ( $\theta$ ) was  $20^\circ$ , consistent with previous studies on broadband SED of this source (e.g., [Abdo et al. 2009](#); [Aleksić et al. 2014](#); [Tanada et al. 2018](#); [Fukazawa et al. 2018](#)). However, this value of  $\theta$  is much smaller than that inferred from radio observations ( $\theta = 30^\circ - 55^\circ$ ; [Walker et al. 1994](#) and  $\theta = 49^\circ - 81^\circ$ ; [Fujita & Nagai 2017](#)). Other derived physical parameters for all the activity states are the blob radius of  $R = 0.14 \times 10^{18}$  cm, the magnetic field of  $B = 0.08$  G and the bulk Lorentz factor  $\Gamma = 3.0$ . These values are in the range considered in previous studies (e.g., [Abdo et al. 2009](#); [Aleksić et al. 2014](#); [Tanada et al. 2018](#); [Fukazawa et al. 2018](#)).

While modelling the S1, S2 and S3 states, the maximum value

of the particle Lorentz factor and the break Lorentz factors were grossly estimated from the observed photon spectrum so that the maximum observed photon frequency and the spectral turn over in the IC hump could be generated. The minimum Lorentz factor was adjusted so that the SSC process could explain the X-ray flux. Nevertheless, with the given data none of these parameters could be constrained well for S1, S2 and S3 states.

While modelling of the SEDs during AS1 and AS2, the primary approach followed to estimate the spectral parameters remained the same. However, for both the states, the soft and hard X-ray spectra appeared in the falling edge of the synchrotron peak. Therefore, the highest frequency of the synchrotron peak and the approximate turnover frequency of the SSC peak were used to estimate the maximum and the break Lorentz factors of the particle spectrum. Nevertheless, they could not be constrained well. Since the spectra moved towards higher energies, the minimum Lorentz factor of the electron distributions was pushed to higher values as compared to the states S1 - S3. The values of the minimum Lorentz factor of electrons comparable to what was obtained for states S1 - S3 would result in more radiation power in the lower frequency region. Therefore, the orders of magnitude of the Lorentz factors that we obtained from the modelling of the SEDs are relatively consistent, even though they are not fully constrained.

The fitted SEDs during S1, S2, and S3 states are shown in Fig 5. SEDs during *AstroSat* observing periods are shown in Fig 6. Due to large error in X-ray flux and photon index values during S1 and AS1 states, we used the derived flux in four bands 1.6 – 3.0, 3.0 – 5.0, 5.0 – 7.0 and 7.0 – 10.0 keV using the “cflux” routine in XSPEC to construct X-ray SED as shown in Fig 5 and Fig 6. The results of our SED fitting are given in Table 7.

Our findings from the SED modelling of S1, S2, S3, AS1 and AS2 states are given below.

- The optical spectral indices during S2 and S3 are steeper than that of X-ray, and  $\gamma$ -rays. Also, the observed flux in the optical band is significantly higher than the predicted flux from the synchrotron emission of the jet electrons. The observed nature of optical flux and spectra suggests that the optical emission might have originated external to the jet, probably from the accretion disk/BLR, host galaxy as well as from the cluster.
- The  $\gamma$ -ray emission was well explained by the SSC emission. The UV emission is marginally higher than that predicted by the synchrotron emission process.
- During S1, S2, and S3 states, the flux in the X-ray band was explained by the SSC emission. However, during AS1 and AS2, X-ray emission was explained by the synchrotron process.
- An increase in jet particle normalisation with no significant variation in other parameters was also noticed during S1, S2, and S3 states. While studying long-term X-ray behaviour of NGC 1275 during 2006-2015, Fukazawa et al. (2018) speculated that increase in the electron density could be one of the possible explanations of the observed long-term X-ray flux increase.
- Unlike S1, S2, and S3 states where energy distribution of jet electrons was very close to a single power-law, a broken power energy distribution of jet electrons, with a much flatter spectrum, was noticed during both AS1 and AS2 observing periods. Also, a significant increase in the minimum and maximum electron Lorentz factors was noticed during *AstroSat* observing periods. The SEDs of the source during AS1 and AS2 show significant changes as compared to the SEDs during S1, S2 and S3 states. First, the overall luminosity of the source increased. Second, the X-ray spectra, as obtained from XRT, SXT and LAXPC, changed the slope during both AS1 and AS2 as compared to the S1, S2 and S3 states. Finally the peak of the SED in synchrotron as well as Compton hump shifted to the higher energies in AS1 and AS2. Therefore the slope of the X-ray spectra during *AstroSat* observing periods indicated that it was part of the synchrotron hump. To model such features in the SEDs of AS1 and AS2 states, it was necessary to increase the values of  $\gamma_1$  and  $\gamma_2$ . The values of  $\gamma_2$  were constrained by both the X-ray and the  $\gamma$ -ray spectra.

#### 4 CONCLUSION

In this work, based on the variation in the  $\gamma$ -ray baseline flux, we identified four activity states of this source. We also observed the source twice with *AstroSat* during its high  $\gamma$ -ray activity state. We found three distinct states (S1, S2, S3) with increase in the  $\gamma$ -ray baseline flux for  $\sim 9$  years, followed by another state (S4) characterised by a large long term  $\gamma$ -ray flare. We determined the boundaries of these activity states by fitting linear functions to the cumulative flux distribution. A correlation study between the  $\gamma$ -ray flux and the spectral nature of the source was carried out. Also, broadband SEDs were constructed and modelled utilising observations from *Fermi*-LAT, *Swift* and *AstroSat*. We conclude:

- An increase of the  $\gamma$ -ray baseline flux with no appreciable change in averaged spectral properties was noticed during S1 to S3 state. Similar behaviour was also noticed in the UV and X-ray bands. An increase in the jet particle normalisation could explain this observed feature.
- No significant correlation was noticed between the  $\gamma$ -ray flux and the spectral parameter/hardness ratio during S1, S2, and S3

states. However, a hint of correlation was noticed during the S4 state.

- Based on the first two years of *Fermi* observations Brown & Adams (2011) reported that “NGC 1275 appeared to migrate from the FR I radio galaxy to the BL Lac object region” during large  $\gamma$ -ray flare. While explaining the steeper X-ray spectrum during 2010 flare of this source, Fukazawa et al. (2018) proposed that the X-ray emission might have synchrotron origin unlike SSC in normal state. In this work, we found that during S1, S2, and S3 states, which represent the long term averaged behaviour of this source, X-ray emission was well explained by the SSC process. However, during AS1 and AS2 observing periods, there is an evidence of an increase in the synchrotron peak frequency and the X-ray emission is explained by the synchrotron emission of jet electrons.

Long term study of NGC 1275 in this work provides a better understanding of the underlying emission mechanism during various activity states.

#### ACKNOWLEDGEMENTS

We thank the anonymous referee for his/her constructive comments that helped us to improve the manuscript considerably. The author(s) thank Ranjeev Misra for discussions regarding *AstroSat*-LAXPC and overall X-ray analysis, and Gulab Dewangan for discussion regarding *AstroSat*-SXT analysis. The author(s) thank Jayashree Roy, Bitan Ghosal, Anil Tolamatti, and Ashish Devaraj (UVIT-POC) for their useful discussions. The author(s) acknowledge the financial support of Indian Space Research Organisation (ISRO) under *AstroSat* archival Data utilization program. This publication uses the data from the *AstroSat* mission of the ISRO, archived at the ISSDC. This work has been performed utilising the calibration data-bases and auxiliary analysis tools developed, maintained and distributed by *AstroSat*-SXT team with members from various institutions in India and abroad. This work has made use of public *Fermi*-LAT data obtained from the *Fermi* Science Support Center (FSSC), provided by NASA Goddard Space Flight Center. This research has made use of the NASA/IPAC Extragalactic Database (NED), which is operated by the Jet Propulsion Laboratory, California Institute of Technology, under contract with the National Aeronautics and Space Administration. This research has made use of data and/or software provided by the High Energy Astrophysics Science Archive Research Center (HEASARC), which is a service of the Astrophysics Science Division at NASA/GSFC and the High Energy Astrophysics Division of the Smithsonian Astrophysical Observatory. This research has made use of the XRT Data Analysis Software (XRTDAS) developed under the responsibility of the ASI Science Data Center (ASDC), Italy. Manipal Centre for Natural Sciences, Centre of Excellence, Manipal Academy of Higher Education (MAHE) is acknowledged for facilities and support.

#### DATA AVAILABILITY

This work has made use of public *Fermi*-LAT data available at <https://fermi.gsfc.nasa.gov/cgi-bin/ssc/LAT/LATDataQuery.cgi>. This research has made use of data and software provided by the High Energy Astrophysics Science Archive Research Center (HEASARC) available at <https://heasarc.gsfc.nasa.gov/docs/software/lheasoft/>, *Swift* data available at <https://heasarc.gsfc.nasa.gov/cgi-bin/W3Browse/w3browse.pl> and the NASA/IPAC Extragalactic

Database (NED). This publication has also made use of the data from the *AstroSat* mission of the ISRO, archived at the ISSDC ([https://astrobrowse.issdc.gov.in/astro\\_archive/archive/Home.jsp](https://astrobrowse.issdc.gov.in/astro_archive/archive/Home.jsp)). *AstroSat* data will be shared on request to the corresponding author with the permission of ISRO.

## REFERENCES

- Abdo A. A., et al., 2009, *ApJ*, **699**, 31
- Abdollahi S., et al., 2020, *ApJS*, **247**, 33
- Acerio F., et al., 2015, *ApJS*, **218**, 23
- Agrawal P. C., 2006, *Adv. Space Res.*, **38**, 2989
- Aleksić J., et al., 2012, *A&A*, **539**, L2
- Aleksić J., et al., 2014, *A&A*, **564**, A5
- Antia H. M., et al., 2017, *ApJS*, **231**, 10
- Arnaud K. A., 1996, in Jacoby G. H., Barnes J., eds, *Astronomical Society of the Pacific Conference Series Vol. 101, Astronomical Data Analysis Software and Systems V*. p. 17
- Asada K., Kamenno S., Shen Z.-Q., Horiuchi S., Gabuzda D. C., Inoue M., 2006, *PASJ*, **58**, 261
- Atwood W. B., et al., 2009, *ApJ*, **697**, 1071
- Baghmanyan V., Gasparyan S., Sahakyan N., 2017, *ApJ*, **848**, 111
- Ballet J., Burnett T. H., Digel S. W., Lott B., 2020, arXiv e-prints, p. [arXiv:2005.11208](https://arxiv.org/abs/2005.11208)
- Benbow W., VERITAS Collaboration 2015, in 34th International Cosmic Ray Conference (ICRC2015). p. 821 ([arXiv:1508.07251](https://arxiv.org/abs/1508.07251))
- Bhattacharya D., Misra R., Rao A. R., Sreekumar P., 2013, *MNRAS*, **431**, 1618
- Bhattacharya D., Mohana A K., Gulati S., Bhattacharyya S., Bhatt N., Sreekumar P., Stalin C. S., 2017, *MNRAS*, **471**, 5008
- Bhattacharya D., Gulati S., Stalin C. S., 2019, *MNRAS*, **483**, 3382
- Bhattacharya D., Mohana A K., Bhattacharyya S., Bhatt N., Stalin C. S., 2021, *MNRAS*, **500**, 1127
- Bhattacharyya S., et al., 2018, *MNRAS*, **481**, 4505
- Brown A. M., Adams J., 2011, *MNRAS*, **413**, 2785
- Bruel P., Burnett T. H., Digel S. W., Johannesson G., Omodei N., Wood M., 2018, arXiv e-prints, p. [arXiv:1810.11394](https://arxiv.org/abs/1810.11394)
- Burrows D. N., et al., 2005, *Space Sci. Rev.*, **120**, 165
- Buttiglione S., Capetti A., Celotti A., Axon D. J., Chiaberge M., Macchetto F. D., Sparks W. B., 2010, *A&A*, **509**, A6
- Cardelli J. A., Clayton G. C., Mathis J. S., 1989, *ApJ*, **345**, 245
- Chitnis V., Shukla A., Singh K. P., Roy J., Bhattacharyya S., Chandra S., Stewart G., 2020, *Galaxies*, **8**, 63
- Churazov E., Forman W., Jones C., Böhringer H., 2003, *ApJ*, **590**, 225
- Ciprini S., 2013, *The Astronomer's Telegram*, **4753**, 1
- Donato D., Wood D., Cheung C. C., 2010, *The Astronomer's Telegram*, **2737**, 1
- Dutton K. L., Edge A. C., Hinton J. A., Hogan M. T., Gurwell M. A., Alston W. N., 2014, *MNRAS*, **442**, 2048
- Falco E. E., et al., 1999, *PASP*, **111**, 438
- Fujita Y., Nagai H., 2017, *MNRAS*, **465**, L94
- Fukazawa Y., et al., 2018, *ApJ*, **855**, 93
- Ghosal B., et al., 2020, *New Astron.*, **80**, 101402
- Godet O., et al., 2009, *A&A*, **494**, 775
- Humason M. L., 1932, *PASP*, **44**, 267
- Imazato F., Fukazawa Y., Sasada M., Sakamoto T., 2021, *ApJ*, **906**, 30
- Kataoka J., et al., 2010, *ApJ*, **715**, 554
- Khachikian E. Y., Weedman D. W., 1974, *ApJ*, **192**, 581
- Kumar A., et al., 2012, in Tadayuki T. Stephen S. M. J. A. d. H., ed., *Proc. SPIE Conf. Ser. Vol. 8443, Space Telescopes and Instrumentation 2012: Ultraviolet to Gamma Ray*. SPIE, Bellingham, p. 84431N
- Kushwaha P., Sinha A., Misra R., Singh K. P., de Gouveia Dal Pino E. M., 2017, *ApJ*, **849**, 138
- MAGIC Collaboration et al., 2018, *A&A*, **617**, A91
- Mattox J. R., et al., 1996, *ApJ*, **461**, 396
- Meyer M., Scargle J. D., Blandford R. D., 2019, *ApJ*, **877**, 39
- Mirzoyan R., 2016, *The Astronomer's Telegram*, **9689**, 1
- Mirzoyan R., 2017, *The Astronomer's Telegram*, **9929**, 1
- Mukherjee R., VERITAS Collaboration 2016, *The Astronomer's Telegram*, **9690**, 1
- Mukherjee R., VERITAS Collaboration 2017, *The Astronomer's Telegram*, **9931**, 1
- Nishino S., Fukazawa Y., Hayashi K., Nakazawa K., Tanaka T., 2010, *PASJ*, **62**, 9
- Pivato G., Buson S., 2015, *The Astronomer's Telegram*, **8219**, 1
- Rani B., Madejski G. M., Mushotzky R. F., Reynolds C., Hodgson J. A., 2018, *ApJ*, **866**, L13
- Rao A. R., Singh K. P., Bhattacharya D., 2016, *Space Research Today*, **196**, 30
- Rao A. R., Bhattacharya D., Bhalerao V. B., Vadawale S. V., Sreekumar S., 2017, *Current Science*, **113**, 595
- Roming P. W. A., et al., 2005, *Space Sci. Rev.*, **120**, 95
- Schlaflly E. F., Finkbeiner D. P., 2011, *ApJ*, **737**, 103
- Schmidt R. W., Fabian A. C., Sanders J. S., 2002, *MNRAS*, **337**, 71
- Singh K. P., et al., 2014, in Tadayuki T. Jan-Willem A. d. H. M. B., ed., *Proc. SPIE Conf. Ser. Vol. 9144, Space Telescopes and Instrumentation 2014: Ultraviolet to Gamma Ray*. SPIE, Bellingham, p. 91441S
- Singh K. P., et al., 2017, *Journal of Astrophysics and Astronomy*, **38**, 29
- Tanada K., Kataoka J., Arimoto M., Akita M., Cheung C. C., Digel S. W., Fukazawa Y., 2018, *ApJ*, **860**, 74
- Tandon S. N., et al., 2017, *AJ*, **154**, 128
- Tandon S. N., et al., 2020, *AJ*, **159**, 158
- Tavecchio F., Ghisellini G., 2014, *MNRAS*, **443**, 1224
- Vadawale S. V., Chattopadhyay T., Rao A. R., Bhattacharya D., Bhalerao V. B., Vagshette N., Pawar P., Sreekumar S., 2015, *A&A*, **578**, A73
- Vermeulen R. C., Readhead A. C. S., Backer D. C., 1994, *ApJ*, **430**, L41
- Walker R. C., Romney J. D., Benson J. M., 1994, *ApJ*, **430**, L45
- Wood M., Caputo R., Charles E., Di Mauro M., Magill J., Perkins J. S., Fermi-LAT Collaboration 2017, *International Cosmic Ray Conference*, **301**, 824
- Yadav J. S., et al., 2016a, *ApJ*, **833**, 27
- Yadav J. S., et al., 2016b, in Jan-Willem A. d. H. Tadayuki T. M. B., ed., *Proc. SPIE Conf. Ser. Vol. 9905, Space Telescopes and Instrumentation 2016: Ultraviolet to Gamma Ray*. SPIE, Bellingham, p. 99051D
- Yamazaki S., et al., 2013, *PASJ*, **65**, 30

This paper has been typeset from a  $\text{\LaTeX}$  file prepared by the author.